Combined Effect of Citrate and Fluoride Ions on Hydroxyapatite Nanoparticles

(Article begins on next page)

29 July 2024

CRYSTAL GROWTH & DESIGN

Article

Combined effect of citrate and fluoride ions on hydroxyapatite nanoparticles

Lorenzo Degli Esposti, Alessio Adamiano, Anna Tampieri, Gloria Belén Ramírez-Rodríguez, Dritan Siliqi, Cinzia Giannini, Pavlo Ivanchenko, Gianmario Martra, Feng-Huei Lin, José Manuel Delgado-López, and Michele Iafisco

Just Accepted

Combined effect of citrate and fluoride ions on hydroxyapatite nanoparticles

Lorenzo Degli Esposti[a], *, Alessio Adamiano[a], Anna Tampieri[a],

Gloria Belen Ramirez-Rodriguez[b], Dritan Siliqi[c], Cinzia

Giannini[c], Pavlo Ivanchenko[d], Gianmario Martra[d], Feng-Huei Lin[e,f],

José Manuel Delgado-López[b], Michele Iafisco[a],*

[a]Institute of Science and Technology for Ceramics (ISTEC),

National Research Council (CNR), Via Granarolo 64, 48018 Faenza

(Italy)

[b]Department of Inorganic Chemistry, University of Granada, Av.

Fuente Nueva, s/n, 18071, Granada (Spain)

[c]Institute of Crystallography (IC), National Research Council

(CNR), Via Amendola 122/O, 70126 Bari (Italy)

[d]Department of Chemistry and Interdepartmental Centre

"Nanostructured Interfaces and Surfaces-NIS", University of

Torino, Via P. Giuria 7, 10125, Torino (Italy)

[e]Department of Biomedical Engineering, National Taiwan

University, 10617 Taipei (Taiwan)

19   [f]Institute of Biomedical Engineering and Nanomedicine, National

20   Health Research Institutes, Keyan Road 35, 35053 Miaoli (Taiwan)

21

22   KEYWORDS

23   Hydroxyapatite, nanocrystals, nano-rods, fluoride,

24   biomineralization, citrate, enamel

25

26   ABSTRACT

27   Citrate and fluoride ions are two constituents of dental enamel

28   hydroxyapatite (HA) nanocrystals. Their individual effect on HA

29   crystallization was already studied, and it was proven that both

30   citrate and fluoride ions regulate HA crystal growth. However, the

31   combined effect of citrate and fluoride ions on HA nanocrystals

32   has never been reported so far. In this work we have prepared

33   citrate-fluoride-HA (citrate-FHA) nanoparticles in mild conditions

34   and we have studied the evolution of morphology and composition

35   upon maturation. We have proved that even in presence of citrate,

36   fluoride ions are incorporated in the apatitic structure

37   (replacing hydroxyl ions) and accelerate the crystallization

38   process. Interestingly, citrate-FHA nanoparticles exhibit a

39   flattened hexagonal rod-like morphology in contrast to the needle-

40   like platelet morphology of citrate-HA. The density of citrate

41   ions bounded on the citrate-FHA surface is higher than that on

42   citrate-HA. Moreover, the relative amount of unidentate citrate-

43   Ca^{2+} adducts *vs* the ionic-like ones is higher for citrate-FHA than

44   for citrate-HA. Our results provide a deeper understanding of the

45   combined effect of citrate and fluoride ions on HA nanocrystals

46   that can be used for the design of advanced biomaterials with

47   tailored features, for a better comprehension of enamel

48   biomineralization process, and for the synthesis of enamel-like

49   nanocrystals.

50

51   1. Introduction

52   It is nowadays widely demonstrated that nanomaterials, in

53   comparison to their bulk counterparts, possess unique and novel

54   properties that could have a huge impact in health, environment,

55   energy and many other technological sectors.

56   Being similar to the mineral phases of bone and teeth, the

57   generation of synthetic hydroxyapatite (HA, $Ca_{10}(PO_4)_6(OH)_2$)

58   nanocrystals is of great interest both to synthesize nanomaterials

59   for the medical field and to mimic *in vitro* the formation of

60   biominerals [1-3]. In addition, HA nanocrystals have recently

61   attracted great attention also as promising materials for

62   applications far from medicine, such as catalysis, water

63   remediation, and agriculture as they represent a more

64   biocompatible and green alternative to the currently used

65   materials [4-6].

66   Several methods have been set-up to prepare HA nanocrystals with

67   tailored size, morphology, surface properties, chemical

68   composition and crystallinity [7-9]. Among them, the strategies

69   that employ organic templates and additives are successful to finely

70   control the structural and morphological features of HA [9, 10].

71   These organic molecules influence the nucleation and crystal

72   growth of HA by interacting with calcium or phosphate ions in the

73   early stage of particle formation, and they can also bind

74   preferentially to specific HA crystal faces inhibiting growth on

75   the respective crystallographic axes [11]. In this respect,

76   biological macromolecules, polymers, amines, amino acids, fatty

77   acids, and small carboxylates have been used to tailor the features

78   of HA nanocrystals [12]. Citrate was widely studied as a "bio-

79   inspired" organic additive in HA synthesis because it is naturally

80   present in bone, enamel and dentin [13, 14]. The strong effect of

81   citrate on HA crystallization has been investigated using

82   complementary techniques such as: powder X-ray diffraction (PXRD),

83   synchrotron wide angle X-ray total scattering (WAXTS) [15], atomic

84   force microscopy (AFM) [15], solid-state nuclear magnetic

85   resonance (ssNMR) [13], IR and Raman spectroscopy [16], and high

86   resolution transmission electron microscopy (HR-TEM) [17]. These

87   studies have proved that citrate plays a dual role in HA

88   crystallization. First, it drives the growth of HA via an amorphous

89   precursor, and second it induces a non-classical oriented

90   aggregation of the nanocrystals [15, 16, 18, 19]. HA nanocrystals

91   synthesized in presence of citrate (citrate-HA) possess a platy

92   morphology, that means to say that the nanocrystals are elongated

93   nano-platelets whose dimensions depend on crystallization time. It

94   has been proposed that the effect of citrate molecules is to bind

95   preferentially to the (1 0 -1 0) HA crystal face, inhibiting its

96   orthogonal growth and making it the predominant one. Furthermore,

97   it was demonstrated that during the early stages of

98   crystallization, citrate-HA grows by an oriented aggregation

99   mechanism through the attachment of the citrate-free (0 0 0 1)

100 faces [19]. Citrate-HA nanocrystals have excellent

101 biocompatibility and colloidal stability [16] and have been tested

102 for biomedical applications as nano-carriers of drugs and imaging

103 agents and as coatings of metallic prostheses [20, 21].

104   HA nanocrystals doped with foreign ions have also raised

105 attention, since ionic substitution is a powerful tool to improve

106 their performances for different applications [22]. For example,

107 doping was widely used to give HA antibacterial or osteoinductive

108 activity, or for providing special properties like luminescence or

109 magnetism [22, 23]. Among biologically relevant ions, fluoride ion

110 (F^-) is of high interest for dental application, since it reduces

5

111 enamel demineralization and inhibits microorganisms in the

112 cariogenic biofilm [24]. Fluoride-doped HA (FHA,

113 $Ca_{10}(PO_4)_6(F)_x(OH)_{2-x}$, $0 < x \leq 2$) has been studied for osteoporosis

114 treatment, as antibacterial biomaterial, for dental enamel

115 protection and remineralization, and for improving the

116 luminescence of rare earth-doped HAs [25-29]. FHA nanocrystals

117 were mainly synthesized by hydrothermal treatments [30, 31] while

118 few works used the wet chemical processes [32, 33]. It was

119 demonstrated that fluorine doping influences HA crystallinity,

120 crystalline domains size, and morphology [22, 33, 34].

121 The feasibility of doping citrate-HA nanocrystals with carbonate,

122 metallic and lanthanide ions and their effect on the chemical-

123 physical features of the resulting materials has been previously

124 studied [16, 20, 35, 36]. Nonetheless, despite the fact that

125 fluoride ion is present in enamel HA crystals of humans and other

126 species [37, 38], the simultaneous effect of citrate and fluoride

127 on HA nanocrystals has never been reported so far.

128 The main aim of this work is the preparation of citrate-FHA

129 nanoparticles in mild conditions and the investigation of the

130 combined effect of citrate and fluoride ions on HA crystal

131 structure evolution as a function of precipitation time. Herein,

132 citrate-FHA nanocrystals were prepared employing a thermal-

133 decomplexing batch reaction at 80°C [16]. The evolution of the

134 physical-chemical, surface and morphological properties of

135 citrate-FHA nanocrystals have been thoroughly characterized upon

136 maturation by using conventional analytical techniques and Small-

137 angle X-ray scattering (SAXS) with synchrotron radiation.

138

139   2. Materials and Methods

140   2.1. Materials

141   Calcium chloride dihydrate ($CaCl_2 \cdot 2H_2O$, ≥99.0% pure), sodium

142 citrate tribasic dihydrate ($Na_3(C_6H_5O_7) \cdot 2H_2O$, ≥99.0% pure (hereafter

143 named $Na_3(Cit)$), sodium hexametaphosphate (($NaPO_3)_6$, ≥96.0% pure),

144 sodium phosphate dibasic dihydrate ($Na_2HPO_4 \cdot 2H_2O$, ≥99.0% pure) and

145 sodium fluoride (NaF, ≥99.0% pure) were purchased from Sigma

146 Aldrich (St. Luis, MO, USA) and used without further purification.

147 All the solutions were prepared with ultrapure water (18.2 MΩ ×

148 cm, 25 °C, Arium© pro, Sartorius).

149

150   2.2. Sample preparation

151   Dry powder citrate-FHA was synthesized by a wet chemical

152 precipitation previously reported by Delgado-López *et al.* [16]

153 with modifications. Namely, two solutions (1:1 v/v, 200 ml total)

154 of (i) 100 mM $CaCl_2$ + 400 mM $Na_3(Cit)$ and (ii) 120 mM Na_2HPO_4 + 50

155 mM NaF were mixed at room temperature. Afterward the mixture was

156 thermostated at 80 °C under stirring in a water bath for three

157 maturation times (5 minutes, 30 minutes, and 4 hours). After

158 maturation the particles were repeatedly washed with ultrapure

159 water by centrifugation at 7000 RPM for 10 minutes and then freeze-

160 dried overnight at -50 °C under a vacuum of 3 mbar. The lyophilized

161 powders were subsequently grinded and sieved with a 50 μm sieve in

162 order to achieve a uniform granulometry. Citrate-HA samples were

163 also prepared as control through the same protocol but without

164 adding NaF into phosphate solution (ii). All the syntheses were

165 performed in triplicates to ensure the reproducibility of the

166 processes. Data are expressed as mean values ± standard deviation

167 (SD) of independent experiments (n = 3).

168

169 2.3. Chemical, morphological and structural characterization

170 Powder X-ray diffraction (PXRD) patterns of the samples were

171 recorded on a D8 Advance diffractometer (Bruker, Karlsruhe,

172 Germany) equipped with a Lynx-eye position sensitive detector

173 using Cu Kα radiation (λ = 1.54178 Å) generated at 40 kV and 40

174 mA. Diffractograms were recorded in the 2θ range from 10 to 80°

175 with a step size (2θ) of 0.02 and a counting time of 1s. Unit cell

176 indexing was performed with the software TOPAS5 [39]. Unit cell

177 axes were obtained by Rietveld refinement considering a single-

178 phase system, using tabulated atomic coordinates of FHA and HA

179 (FHA: PDF card 00-015-0876, HA: PDF card 00-055-0592) [33, 40].

180 Symmetrized spherical harmonics were used to cope,

181 phenomenologically, with anisotropic peak broadening effects due

182   to the anisotropic crystal shape. The PXRD patterns background was

183   calculated as 11-th order Chebychev function.

184   The average size of crystal domains along the apatite axis

185   directions ($D_{[0002]}$) and ($D_{[31\text{-}40]}$) were calculated as full-profile

186   peak broadening evaluation with the software TOPAS5, using

187   fundamental parameters peak function. Instrumental peak broadening

188   was evaluated by collecting a standard LaB_6 sample before the

189   analysis.

190   Fourier transform infrared (FT-IR) spectroscopy analyses of bulk

191   modes were carried out on a Nicolet iS5 spectrometer (Thermo Fisher

192   Scientific Inc., Waltham, MA, USA) with a resolution of 2 cm^{-1} by

193   accumulation of 64 scans, using a diamond ATR accessory model iD7.

194   FT-IR spectroscopy in a controlled atmosphere mode was used for

195   inspecting surface citrates. To this aim, nanoparticles were

196   pressed in the form of self-supporting pellets and placed into an

197   IR cell equipped with KBr windows and connected to a conventional

198   vacuum line (residual pressure 5×10^{-4} mbar), allowing

199   adsorption/desorption experiment to be carried out *in situ*. The IR

200   spectra were collected in the transmittance mode with an Equinox

201   55 spectrometer (Bruker, Karlsruhe, Germany) equipped with a DTGS

202   detector (128 scans; resolution: 4 cm^{-1}). Because the target was

203   the citrate spectral pattern in the 1720-1320 cm^{-1} range, the δH_2O

204   band due to possibly co-adsorbed water molecules was shifted below

205   the lower limit of this range by exchanging H_2O molecules with D_2O

206 ones (δD_2O at ca. 1200 cm^{-1}). Details on the experimental procedure,

207 as well as the spectra collected at each step, finally resulting

208 in data reported Figure 3 in the following, are reported in the

209 Supporting Information.

210 Raman spectra were collected with a LabRAM-HR spectrometer with

211 backscattering geometry (Jobin-Yvon, Horiba, Japan). The

212 excitation line was provided by a diode laser emitting at a

213 wavelength of 532 nm and a Peltier cooled charge-couple device

214 (CCD) (1064x256 pixels) was used as detector. Spectrometer

215 resolution was better than 3 cm^{-1}. The final spectrum resulted by

216 the average of 3 acquisitions (acquisition time = 300 s).

217 Transmission electron microscopy (TEM) evaluation was performed

218 with Tecnai F20 microscope (Fei Corp., Hillsboro, OR, USA)

219 operating at 120 kV. The powder samples were ultrasonically

220 dispersed in ultrapure water and then a few droplets of the slurry

221 were deposited on 200 mesh copper TEM grids covered with thin

222 amorphous carbon films and incubated for several minutes.

223 Nanoparticle morphology analysis was performed with software

224 ImageJ [41].

225 Scanning transmission electron microscopy (STEM) images and

226 compositional analysis (Ca, P and F) of selected areas were

227 acquired with a FEI TITAN G2 microscope operating at 300 kV

228 equipped with a HAADF detector and a SUPER-X Energy dispersive X-

229 ray (EDS) detector (Centre for Scientific Instrumentation,

230   University of Granada). FHA nanoparticles were dispersed in pure

231   ethanol and some drops of the slurry were deposited on 200-mesh

232   copper grids with lacey carbon films.

233   Scanning electron microscopy (SEM) evaluation was performed with

234   field-emission microscope (FEG-SEM, mod. ΣIGMA, ZEISS NTS Gmbh, Oberkochen, Germany)

235   with in-lens acquisition mode, operating at 3 kV acceleration voltage, with a working

236   distance of 1.7mm. The powder samples were ultrasonically dispersed at

237   a concentration of 0.1mg/mL in 10 mL of a 0.01 wt.% sodium

238   hexametaphosphate aqueous solution, sonicating it with a tip

239   sonicator (Vibracell VCX 500 with 13mm sonicating tip, SONICS,

240   Newtown, CT, USA) under ice cooling with the following working

241   parameters: 20% amplitude, 3 minutes, pulsation 5s on / 5s off.

242   Afterward, a drop of the stabilized particle suspension was

243   deposited on a flat, mirror polished silicon wafer mounted on an

244   aluminum stub and left to dry at room temperature. After drying

245   the samples was sputter-coated (Polaron E5100, Polaron Equipment,

246   Watford, Hertfordshire, UK) with 2nm of Pt/Pd (80:20) alloy in

247   order to provide electrical conductance.

248   Quantification of Ca and P was carried out by inductively coupled

249   plasma atomic emission spectrometer (ICP-OES) (Agilent

250   Technologies 5100 ICP-OES, Santa Clara, CA, USA) while F was

251   quantified with a fluoride ion electrode (Intellical™ ISEF121,

252   Hach Lange, Loveland, CO, USA). Samples were prepared by dissolving

253   an aliquot of powder in a 1 wt. % HNO_3 solution.

254   Thermogravimetry analyses (TGA) were performed using a STA 449F3

255   Jupiter (Netzsch GmbH, Selb, Germany) apparatus. About 10 mg of

256   sample was weighted in an alumina crucible and heated from room

257   temperature to 1100 °C under air flow with a heating rate of 10

258   °C/min.

259   Surface charge of the samples was evaluated by electrophoretic

260   mobility (ζ-potential) using a Zetasizer Nano analyzer (Malvern,

261   UK). Citrate-HA and citrate-FHA nanocrystals 0.5 mg/mL aqueous

262   suspensions at pH ≈ 7.0 were measured using disposable folded

263   capillary cells (DTS1061; Malvern, UK) at 25°C. Three separate

264   measurements (100 runs each) were collected in each case.

265   Specific surface area (SSA) of the powdered samples was measured

266   through N_2 gas adsorption modeled by the Brunauer–Emmett–Teller

267   (BET) method [42]. BET N_2 gas adsorption method was employed using

268   a Surfer instrument (Thermo Fisher Scientific Inc., Waltham, MA,

269   USA). Before the measurement, the samples were pre-treated at 100°C

270   for 3 hours under vacuum.

271   Small Angle X-ray Scattering (SAXS) measurements were performed

272   at the high brilliance Austrian SAXS beamline of the ELETTRA

273   Synchrotron (Trieste, Italy). The available q-range was 0.08 to

274   about 6 nm^{-1} using an incident beam energy of 8 keV. A two-

275   dimensional (2D) scattering image was acquired within 100 ms with

276   a Pilatus 1 M detector (Dectris, CH). The samples were measured at

277   room temperature in glass capillaries of 1.5 mm diameter (WJM-

278   Glas/Müller GmbH, Berlin-Pankow, DE). As a first step, the

279   scattering from the air and the sample holder was collected to be

280   subtracted as background. The data reduction was done by the freely

281   available   software   of   the   beamlines   Fit2D   [43].   The   two-

282   dimensional data were circularly averaged to convert them into

283   one-dimensional   scattering   curves.   Nine   different   scattering

284   curves   were   collected   for   each   sample   and   consequently   were

285   averaged and background corrected. From the experimental curves,

286   the   modeling   was   performed   by   using   SasView   package   V4.2.2

287   (www.sasview.org).   We   estimated   the   averaged   particle   size   for

288   selected models, and as well as an estimation of the polydispersity

289   of the samples, by using Schulz distribution [44, 45], which is

290   the most indicated to describe particle sizes. SAXS data was fitted

291   with the lamellar model as previously described [46].

292

293   3. Results and discussion

294

295   3.1 Powder X-Ray Diffraction (PXRD) characterization

296   PXRD patterns of citrate-FHA samples show the typical diffraction

297   peaks of FHA as single phase (PDF card file 00-015-0876) (Figure

298   1A). In particular, the most intense reflections are the narrow

299   peak at 25.87° due to the (0 0 0 2) crystallographic planes and

300   the broad peak centered at about 32° that is the sum of three peaks

301   at 31.77°, 32.19°, and 32.90°, due to planes (2 1 -3 1), (1 1 -1

302 2), and (3 0 -3 0). Other peaks are present at 39.81°, 46.71°,

303 49.46°, and 53.14°, which correspond to the planes (3 1 -4 0), (2

304 2 -4 2), (2 1 -3 3), and (0004), respectively [20]. In all the

305 samples, the diffraction peaks are broad and poorly defined,

306 indicating the presence of nanocrystals with reduced crystal

307 domains and crystalline order in all the samples [16]. The PXRD

308 patterns of citrate-FHA 5m show particularly broad peaks, while

309 the patterns of the samples prepared at longer maturation time

310 present sharper peaks. This behavior reveals an increase of

311 structural order and crystal growth upon maturation. Citrate-FHA

312 peaks are better defined than the corresponding citrate-HA peaks

313 (Figure S1A) in all time points, suggesting that citrate-FHA

314 crystal domains are always more ordered and larger in size than

315 those of citrate-HA. The increase of HA crystallinity as a function

316 of the incorporation of fluoride ions has been widely reported

317 [34, 47, 48] and this was attributed to a higher affinity of

318 fluoride ions for HA crystal lattice in comparison to hydroxyl

319 ions, which decreases lattice strain and enhances thermodynamic

320 stability.

321

322
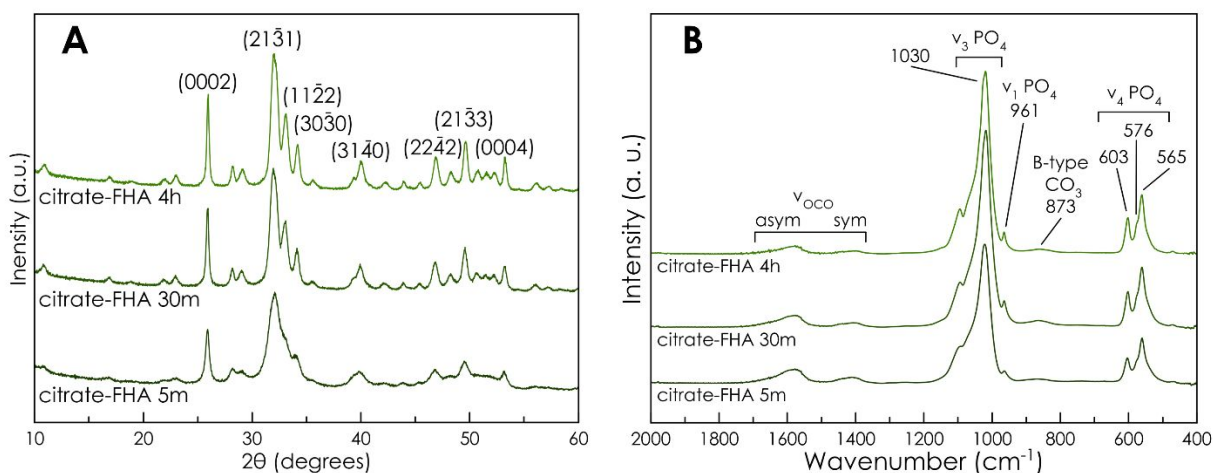
Figure 1. (A) PXRD patterns and (B) IR-ATR of citrate-FHA 5m, citrate-FHA 30m, and citrate-FHA 4h.

The evaluation of unit cell parameters calculated by Rietveld refinement of PXRD data show that the *a* unit cell parameters of citrate-FHA samples (Table 1 and Figure S2) are always notably shorter than those of citrate-HA (Table S1) while the *c* unit cell parameters are comparable. A shortening of the *a* cell axis of ca. 0.005 nm was reported for FHA. This was attributed to the shorter Ca-F equilibrium distance compared to the Ca-OH distance of HA [32, 49]. It was previously demonstrated that carbonate doping influences HA unit cell parameters [15], however taking into account that the carbonate content and position in the crystal lattice is similar for citrate-FHA and citrate-HA (see data below) it is likely that the presence of carbonate is not the cause of the different crystallographic properties of the two materials.

340   The unit cell parameters of both materials shrink at increasing

341   maturation time (Figure S2). The unit cell parameters of citrate-HA

342   calculated herein are close to those previously reported [15].

343   Sizes of the crystal domains were estimated along the $D_{(0001)}$ and

344   $D_{(hki0)}$ directions, being parallel to the longest and the shortest

345   axes of the hexagonal unit cell, respectively. To this aim, the

346   broadening of the non-overlapped (0 0 0 2) and (3 1 -4 0)

347   reflections were used, and the results are shown in Table 1 (and

348   Figure S3). The average size of crystal domains of citrate-FHA

349   along the c-axis ($D_{(0002)}$) and along the a–b plane ($D_{(31-40)}$) are both

350   larger than the corresponding crystal domains of citrate-HA for

351   each maturation time (Table S1) [16]. Similarly to citrate-HA,

352   also $D_{(0002)}$ values of citrate-FHA are higher than those of $D_{(31-40)}$,

353   indicating that the crystals are elongated along the c-axis.

354   Interestingly, the aspect ratio estimated as $D_{(0002)}/D_{(31-40)}$ remains

355   constant with maturation for citrate-FHA, while it increases over

356   time for citrate-HA. All together, these data suggest that citrate-

357   FHA crystal domains are larger in size than citrate-HA ones in all

358   time points and that the crystal growth is faster in the presence

359   of F⁻, as suggested by the higher slope of the graph of the crystal

360   domain dimensions vs time (Figure S3). The other striking

361   difference is the isotropic growth of citrate-FHA (i.e. $D_{(0002)}/D_{(31-}$

362   $_{40)}$ remains constant) versus the preferential crystal growth along

363   c-axis for citrate-HA.

364

Table 1. Cell parameters and crystal domain sizes of citrate-FHA

366　samples.

Sample	$a-b$ cell axes (Å)	c cell axis (Å)	$D_{(0002)}$ (nm)	$D_{(31-40)}$ (nm)	$D_{(0002)} / D_{(31-40)}$
Citrate-FHA 5m	9.413	6.894	24.7±0.5	9.4±1.6	2.6
Citrate-FHA 30m	9.398	6.886	42.4±0.8	14.1±0.9	3.0
Citrate-FHA 4h	9.390	6.885	56.9±1.1	20.4±0.9	2.8

367

368

369　3.2 Compositional analysis

370　The chemical composition and surface charge of citrate-FHA

371　samples are reported in Table 2. The Ca/P ratio of the citrate-

372　FHA nanocrystals is higher and closer to the stoichiometric value

373　(i.e. 1.67) than citrate-HA (Table S2), which is in agreement with

374　the higher structural order of FHA. The increase of Ca/P ratio as

375　a function of the incorporation of fluoride ions due to increased

376　structural order has been already reported [32, 49]. Ca/P ratio as

377　well as fluoride content (about 3 wt. %) does not vary upon

378　maturation. The Ca/F ratio of citrate-FHA samples is slightly lower

379　than the value of stoichiometric fluorapatite (Ca/F = 5 for

380　$Ca_{10}(PO_4)_6(F)_2$). All the samples present a small amount of carbonate

381 and citrate ions, that was evaluated by TGA-DTG analysis as

382 previously described (Figure S4) [50]. The occurrence of carbonate

383 ions is mainly due to dissolved CO_2 in the mother solution and its

384 amount is similar in citrate-FHA and citrate-HA samples (about 1

385 wt.%).

386 Interestingly, citrate-FHA has a lower weight content of citrate

387 than citrate-HA at each maturation time. The amount of citrate in

388 the citrate-FHA samples decreases during the first 30 minutes of

389 maturation and then it remains stable. On the other hand, the

390 amount of citrate constantly decreases up to 24 hours of maturation

391 time for citrate-HA samples [16]. This continuous decrease of

392 citrate content upon maturation has been previously attributed to

393 a gradual dissolution of the surface non-apatitic hydrated layer

394 [16] which, as described by Rey *et al.* [51], is well present in

395 freshly formed precipitates but progressively disappears as the

396 stable apatitic crystalline domains develop upon maturation. It

397 was also suggested that upon drying a partial restructuration of

398 the surface hydrated layer occurs, but part of the non-apatitic

399 environments still remains [51]. The ζ-potential of all the samples

400 at pH 7.0 is negative, due to the presence of citrate ions on

401 nanocrystals surface [52]. Citrate-FHA possesses a surface charge

402 that is slightly more negative than citrate-HA in all time points

403 (Table S2), in agreement with its higher density of citrates on

404 the surface in comparison to citrate-HA (see below). Overall, the

405 ζ-potential of the samples becomes less negative upon maturation.

406 This trend is likely associated with the decrease of citrate

407 content [16].

408

409

410 **Table 2.** Chemical composition of citrate-FHA samples.

Sample	Ca/P[a]	F[b] (% wt)	Ca/F[a,b]	Citrate[c] (% wt)	Carbonate[c] (% wt)	ζ-Potential (mV)
Citrate-FHA 5m	1.60±0.01	3.1±0.2	4.4±0.5	3.2±0.4	1.1±0.1	-15.2 ± 0.4
Citrate-FHA 30m	1.58±0.01	3.0±0.1	4.6±0.2	1.8±0.2	0.9±0.1	-14.3 ± 0.3
Citrate-FHA 4h	1.59±0.01	3.0±0.1	4.6±0.2	1.8±0.2	1.0±0.1	-11.1 ± 0.4

411 [a]Quantified by ICP-OES; [b]Quantified by fluoride ion electrode;
412 [c]Quantified by TGA.

413

414

415 3.3 Spectroscopic characterization

416 The IR-ATR spectra of the citrate-FHA samples are reported in

417 Figure 1B. All samples displayed a main broad band at 1030 cm^{-1}

418 with shoulders at 1046 and 1075 cm^{-1} due to the triply degenerated

419 antisymmetric stretching mode of the apatitic PO$_4$ groups (ν_3PO$_4$).

420 Other features emerge at 961 cm^{-1} (symmetric stretching mode of the

421 apatitic PO$_4$ groups, ν_1PO$_4$) and at 603, 576 (as a shoulder) and

422 565 cm^{-1} (triply degenerated bending mode of the same groups,

423 $\nu_4 PO_4$). The absence of the band associated to hydroxyl ions at 631

424 cm^{-1} [53], that is present in the IR-ATR spectra of citrate-HA

425 samples (Figure S1B), suggests the almost complete substitution of

426 the OH^- groups by F^- in the crystal lattice, as it was previously

427 reported in other FHA samples [47, 49]. The presence of trace

428 amounts of carbonate ions detected by TGA analysis was confirmed

429 by a very weak B-type carbonate substitution (CO_3 occupying PO_4

430 sites) band at 873 cm^{-1} [54]. Equivalent information was obtained

431 by Raman spectroscopy investigation (Figure S5 and related

432 comments in Supporting Information).

433 The understanding of the interaction of citrate ions with

434 nanocrystals surface is of particular interest. Previous

435 investigation was performed on citrate-HA 4h through the use of IR

436 spectroscopy under controlled atmosphere [55]. The same approach

437 was adopted here for the investigation of citrate groups at the

438 surface of citrate-FHA 4h.

439 Figure 2 shows a comparison between the spectra in the 1720 –

440 1320 cm^{-1} range of citrate-HA (curve a) and citrate-FHA (curve b)

441 outgassed at beam temperature (b.t.). The data were collected after

442 a complete exchange of surface H_2O molecules with D_2O ones in order

443 to remove the possible contribution of the δH_2O mode from the

444 spectral pattern. This method was preferred to water desorption by

445 outgassing at higher temperature (ca. 423 K, ref. [55]) in order

446 to avoid any possible modification of surface citrates. The spectra

447   of citrate-FHA and citrate-HA are constituted by two sets of

448   components, one in the 1700 - 1500 cm^{-1} range and the second in

449   1460-1325 cm^{-1} range. Because carbonate ions are present in this

450   material in trace amounts (see above), it is expected that they

451   should not contribute significantly to this pattern, which is

452   attributed to the antisymmetric and symmetric stretching modes of

453   carboxylate moieties ($\nu_{asym}COO$ and $\nu_{sym}COO$), respectively. In more

454   detail, in the previous study it was found that $\nu_{asym}COO$ signal can

455   result from the overlapping of two sub-bands at 1592 and 1560 cm^{-1}

456   , which paired with the $\nu_{sym}COO$ components can account for the

457   presence of COO^- groups coordinated to surface Ca^{2+} ions in

458   unidentate way, accompanied by a lower amount of COO^- – Ca^{2+} adducts

459   with an ionic-like structure. Likely, these latter can be due to

460   the citrate molecules remaining in the surface hydrated layer.

461   The spectral profile of citrate-FHA 4h shows a higher overall

462   intensity in comparison to citrate-HA. Being the spectra

463   normalized by either sample mass and specific surface area (details

464   in the SI and in Figure S6), such a difference well accounts for

465   the higher density of citrates on citrate-FHA 4h (ca. 0,71 cit/nm^2)

466   than on citrate-HA 4h (ca. 0,52 cit/nm^2), resulting from the two-

467   fold lower SSA of citrate-FHA 4h (81 ± 8 m^2 g^{-1}) with respect to

468   citrate-HA 4h (160 ± 10 m^2 g^{-1}, as reported in ref. [55]).

469   Noteworthy, the two patterns are also different in shape,

470   indicating the occurrence of differences in the coordination of

471   citrates to surfaces of citrate-FHA or citrate-HA. In particular,

472   the subtraction between the two spectra (curve c = b-a) highlights

473   that their difference is mainly due to the higher intensity of one

474   pair of components at 1572 and 1383 cm^{-1}, that, on the basis of

475   their spectral separation (212 cm^{-1}), can be assigned to unidentate

476   COO^{-} – Ca^{2+} adducts, more abundant on citrate-FHA 4h than on

477   citrate-HA 4h.

478

479
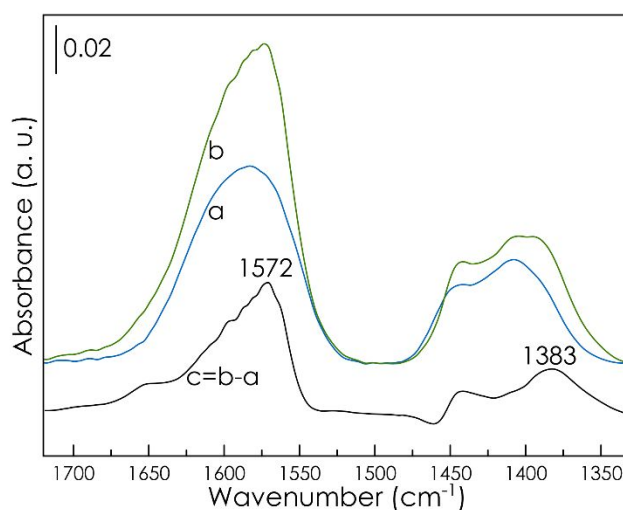
480   **Figure 2.** FT-IR spectra of citrate-HA 4h (a) and citrate-FHA 4h

481   (b) after exchange with D$_2$O and subsequent 60 min outgassing at

482   b.t., the spectra are normalized by mass of sample and SSA of the

483   material; curve (c) resulting from the difference (b)-(a).

484

485   3.4 Morphological characterization

486   TEM micrographs of citrate-FHA nanocrystals are shown in Figure

487   3A-C. Citrate-FHA 5m nanocrystals consist of irregular, small

488   nanoparticles that aggregate in elongated formations. Citrate-FHA

489   30m is composed of elongated particles with better-defined border

490   and with increased crystallinity, as evidenced by the increased

491   presence of spots in the SAED pattern (Figure 3B). Finally, TEM

492   micrographs of citrate-FHA 4h show highly regular crystalline

493   nanoparticles with a rod-like morphology, having an average length

494   of 60 ± 20 nm and an average width of 20 ± 4 nm (Figure 3C).

495   Differently, previously reported TEM analyses have demonstrated

496   that citrate-HA evolves from aggregated amorphous or very poorly

497   crystalline particles to thin needle-like nanoparticles [16, 55].

498   The rod-like morphology of citrate-FHA 4h was never observed in

499   citrate-HA, neither in citrate-HA doped with carbonate, europium

500   nor other metal cations. On the other hand, rod-like FHA

501   nanoparticles were reported in the case of FHA prepared through a

502   hydrothermal process [30, 56] or in the presence of Tween 80

503   surfactant [57]. In the former case, the rod-like shape is likely

504   due to the high-energy crystallization conditions that induce the

505   formation of the most thermodynamically stable crystal, which for

506   FHA is a hexagonal prism morphology identical to the unit cell

507   symmetry. In the latter case, it is likely that the surfactant has

508   no preferential faces for adsorption, therefore all the six

509   hexagonal (1 0 0 0) faces are equally inhibited and grow

510   isotropically. In a previous report HA was prepared in presence of

511   both citrate and fluoride ions through a hydrothermal process [56].

512   In this case, particles appeared as dumbbell-shaped microcrystals

513   and did not present the rod-like morphology of the nanoparticles

514   prepared herein.
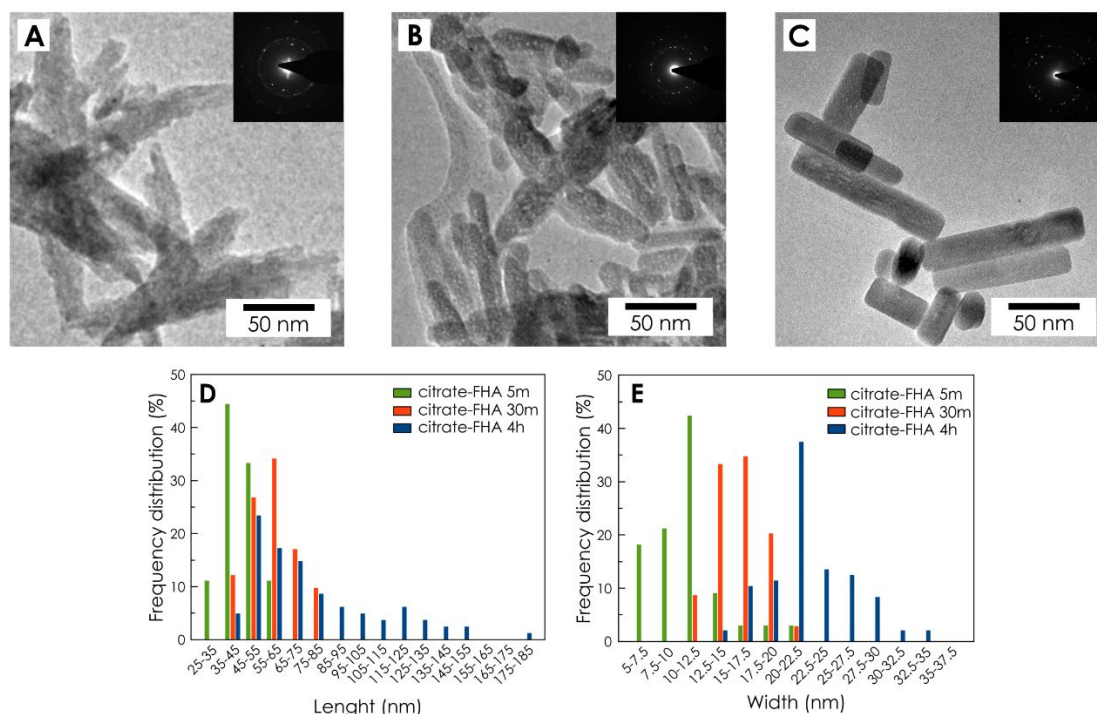
515

516

517

518   **Figure 3.** (A-C) TEM micrographs of (A) citrate-FHA 5m, (B) citrate-

519   FHA 30m and (C) citrate-FHA 4h. Insets show the relative SAED

520   pattern. (D-E) Histograms of the distributions of (D) width and

521   (E) length of citrate-FHA 5m, citrate-FHA 30m, and citrate-FHA 4h

522   (blue bars).

523

524   The mean length (L) along the longest axis, the mean width (W)

525 orthogonal to L, and the aspect ratio (the ratio between L and W)

526 of citrate-FHA nanocrystals were estimated from TEM observations

527 and they are reported in Table 3. L and W values of citrate-FHA

528 increase with maturation time, while the L/W values remain almost

529 constant. The increase over time of the mean size of nanoparticles

530 evaluated by TEM follows the same trend of crystals domains

531 calculated from PXRD data (Figure S7).

532

533 **Table 3.** Mean length (L), mean width (W), and aspect ratio (L/W)

534 of citrate-FHA nanoparticles.

Sample	L (nm)	W (nm)	L/W
Citrate-FHA 5m	39.5 ± 9.6	10.8 ± 3.5	3.7
Citrate-FHA 30m	53.7 ± 10.2	15.6 ± 2.3	3.4
Citrate-FHA 4h	76.9 ± 40.1	22.5 ± 4.6	3.4

535   Measured from TEM micrographs. The mean value and the standard
536 deviation were calculated measuring the sizes of 100 particles
537 from different experiments.

538

539   Figure 3D-E represents the histograms of the distribution of

540 length and width of citrate-FHA nanoparticles synthesized at

541 different maturation times. Both length and width of the particles

542 with highest frequency distribution increased as a function of

543 maturation time. Interestingly, length distribution of citrate-

544 FHA 4h was spread in a wide range (from 30 to 180 nm) (Figure 3D).

545 This high spreading of length values explains the higher error

546 associated to mean value of L for citrate-FHA 4h. Comparing the

547 length and width frequency distribution of citrate-HA 4h

548 nanoparticles previously reported [19], with those of citrate-FHA

549 4h, it is worth to notice that this latter has both a bigger

550 average particle length and a bigger average particle width. In

551 particular, citrate-FHA 4h and citrate-HA 4h are remarkably

552 different in particle width.

553 To   investigate   the   chemical   composition   of   citrate-FHA

554 nanocrystals, STEM-HAADF analysis was performed on citrate-FHA 4h

555 (Figure 4). The EDS spectrum of a selected region (Figure 4A')

556 show the presence of Ca, P, O, and F, which further confirmed the

557 fluoride doping in citrate-FHA. It may be noted that Cu signals

558 observed in the EDS spectra are due to the sample holder used in

559 the analysis. Elemental mapping of Ca, P, and F was performed for

560 a detailed distribution of atomic content of the nanocrystals

561 (Figure 4B-D). The STEM-HAADF chemical maps show a homogeneous

562 distribution of all these elements in the nanocrystals. This

563 finding is consistent with the presence of fluorine ions in the

564 crystal structure of citrate-FHA indicated by IR-ATR and XRD data.
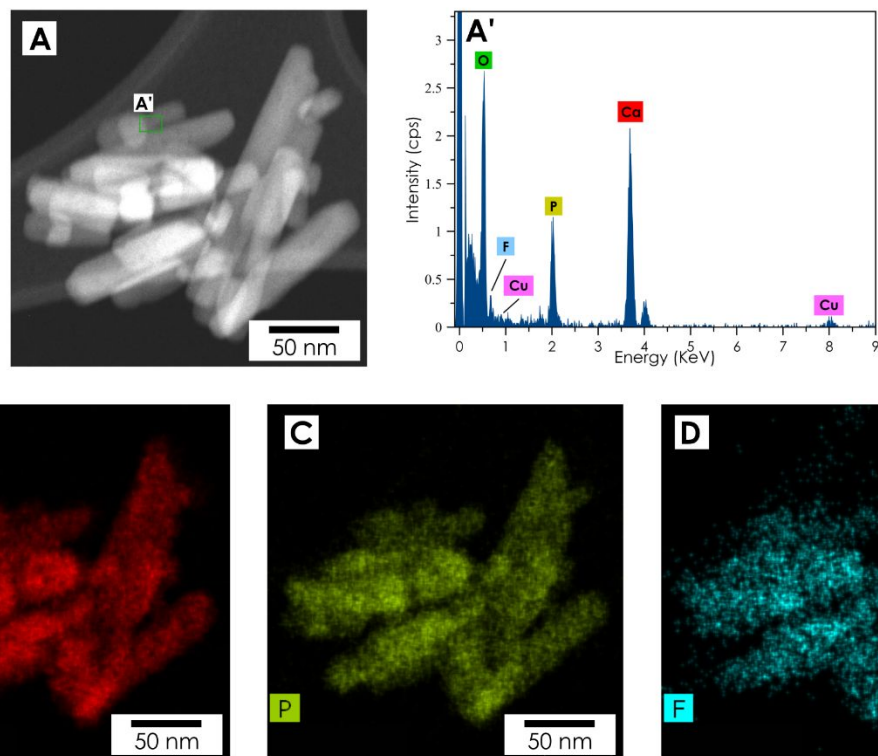
565

566

Figure 4. (A) STEM-HAADF micrograph of citrate-FHA 4h, (A') EDS spectrum from area marked in (A), and chemical maps of Ca (B), P (C), and F (D) from the same micrograph reported in (A). In (A'), the Cu peaks are due to the sample holder.

571

 Representative high-resolution TEM (HR-TEM) micrographs of citrate-FHA 4h are reported in Figure 5. In citrate-FHA 4h lattice fringes spaced at ca. 0.815 nm run uninterrupted for the whole nanocrystal (Figure 5A and magnification A'). This lattice fringe value corresponds to the distance of the (1 0 -1 0) plane of FHA (PDF card file 00-015-0876), indicating that the crystals are elongated along the *c*-axis. Moreover, some facets of the a(b)-

579   planes (e.g., (0 -1 1 0) facet in Figure 5B and magnification B')

580   exhibited stepped surfaces, likely suggesting a classical layer-

581   by-layer growth. Interestingly, in few cases lattice fringes

582   spaced at ca. 0.344 nm with a hexagonal pattern were observed,

583   suggesting that for these particles the *c*-axis was parallel to the

584   electron beam during the image acquisition (Figure 5A,

585   magnification A'') [58]. Therefore, in these cases nanocrystal

586   width and thickness (T) was estimated, suggesting a W/T ratio of
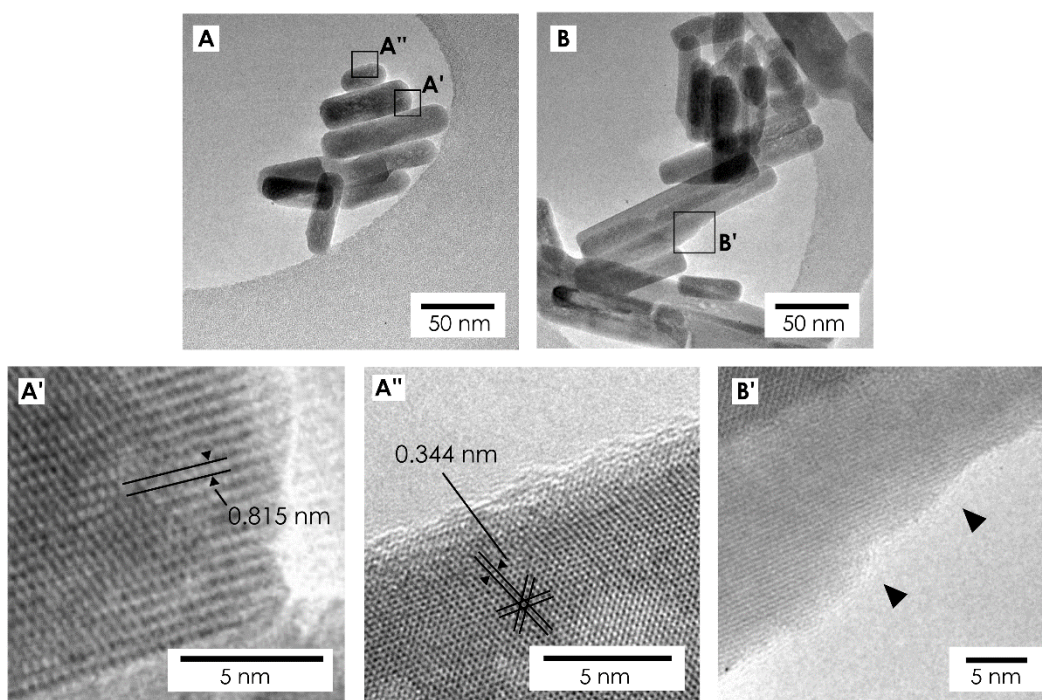
587   ca. 2.

588

589

Figure 5. HR-TEM micrographs of citrate-FHA 4h. A', A'', and B'

correspond to the high magnification of the portions enframed

within the black squares in micrographs A and B, respectively.

593   (A') 0.815 nm fringes that run along citrate-FHA 4h nanocrystal

594   length, (A'') hexagonal fringe pattern with 0.344 spacing, and

595   (B') stepped surfaces (marked by arrows) along *a–b* planes.

596   Citrate-FHA 4h and citrate-HA 4h were analyzed also by FEG-SEM at

597   high magnification (Figure S8). Micrographs show that the samples

598   have a different morphology, namely, citrate-FHA 4h are rods

599   (Figure S8A), while citrate-HA 4h appear as thin needles (Figure

600   S8B).

601   Citrate-FHA and citrate-HA nanoparticles were evaluated by SAXS

602   with synchrotron radiation (Figure S9). The two materials present

603   different SAXS curve shapes. A lamellar model was used to fit the

604   SAXS data providing the values of thicknesses and the corresponding

605   polydispersity (Table 4 and Table S3).

606

607   **Table 4.** Mean thickness and polydispersity of citrate-FHA samples

608   extracted as lamellar model fitting SAXS data.

Sample	Thickness (nm)	Polydispersity
Citrate-FHA 5m	8.9	0.70
Citrate-FHA 30m	7.1	0.32
Citrate-FHA 4h	11.3	0.63

609

610

611   Thickness of citrate-FHA is larger than citrate-HA nanoparticles,

612   in particular at 4 hours of maturation. The thickness of citrate-

613   FHA 4h extracted by SAXS is comparable to the values measured by

614   HR-TEM, thus validating the W/T ratio estimated by the latter

615   technique. The isotropy of citrate-FHA 4h (evaluated as W/T ratio)

616   was compared to the one of citrate-HA 4h previously analyzed [15].

617   The W/T ratio of citrate-FHA 4h (ca. 2) is notably lower than the

618   one of citrate-HA 4h (ca. 6). This result confirms that citrate-

619   FHA and citrate-HA nanocrystals are different, where the former

620   has a flattened rod morphology, in contrast to the thin platelet

621   morphology of the latter.

622   Interestingly,   the   rod-like   morphology   of   citrate-FHA

623   nanoparticles reported in this work are similar to the rod-like

624   enameloid nanocrystals of shark teeth, that contain a high fluorine

625   amount (about 3-5 wt.%, comparable to citrate-FHA), in contrast to

626   the platy enameloids of puffer fish having a much lower fluorine

627   content in teeth (about 0,2 wt.%) that resemble citrate-HA [59].

628

629

630   5. Conclusions

631   In this paper we have studied the combined effect of citrate and

632   fluoride ions on HA in terms of crystal growth, structure and

633   morphology, since only their individual effects were previously

634   investigated.

635   Herein, we have found that even in presence of citrate fluoride

636   ions substitute for OH⁻ and accelerate the crystallization process.

637   The presence of fluoride ions induces a shrinkage of the *a* unit

638   cell parameter of ca. 0.005 nm, a progressive decrease in unit

639   cell parameters, and a concomitant increase of crystal domains as

640   a function of maturation time.

641   Citrate-FHA nanocrystals have a flattened hexagonal rod-like

642   morphology in contrast to the elongated platy morphology of

643   citrate-HA. Indeed, citrate-FHA nanocrystals are elongated too,

644   but their growth is isotropic along all axes of the hexagonal unit

645   cell and without changes in their aspect ratio. Conversely, the

646   growth of citrate-HA nanocrystals is anisotropic, as the growth

647   along the *c*-axis is progressively faster than along normal

648   directions, yielding needle-like nanocrystals.

649   The density of citrate ions bounded on the citrate-FHA surface

650   is higher than that on citrate-HA. Moreover, IR spectra indicated

651   that the relative amount of unidentate citrates *vs* the ionic-like

652   ones is higher for citrate-FHA in comparison to citrate-HA.

653   The data reported in this work are highly relevant to attain a

654   deeper understanding of the combined effect of citrate and fluoride

655   on HA nanocrystals for designing advanced biomaterials with

656   tailored features, for a better understanding of the enamel

657   biomineralization process, and to produce enamel-like

658   nanocrystals. Based on the obtained results, future studies will

659 focus in elucidating the interaction of citrate ions with citrate-

660 FHA surface through computational modeling and in the

661 determination of the mechanical and biological properties of

662 citrate-FHA nanorods.

663

664 ASSOCIATED CONTENT

665 **Supporting Information.** Crystallographic data, TGA analysis

666 interpretation, IR-ATR spectra, Raman spectra, experimental

667 details of FT-IR spectroscopy in controlled atmosphere, SEM

668 micrographs, and SAXS data fitting are supplied as Supporting

669 Information available free of charge (word file).

670 AUTHOR INFORMATION

671 **Corresponding Author**

672   *Dr. Michele Iafisco, Ph. D.

673 Institute of Science and Technology for Ceramics (ISTEC) National

674 Research Council (CNR),

675 Via Granarolo 64, 48018 Faenza (RA), Italy.

676 E-mail: michele.iafisco@istec.cnr.it

677   *Lorenzo Degli Esposti, M. Sc.

678 Institute of Science and Technology for Ceramics (ISTEC) National

679 Research Council (CNR),

694

695   ABBREVIATIONS

696   HA, hydroxyapatite; FHA, fluorine-doped HA; PXRD, powder x-ray

697   diffraction; WAXTS, wide angle x-ray total scattering; AFM,

698   atomic force microscopy; ssNMR, solid-state nuclear magnetic

699   resonance; TEM, transmission electron microscopy; HR-TEM, high

700   resolution transmission electron microscopy; STEM-HAADF,

701   scanning transmission electron microscopy with high-angle

702   annular dark-field detector; FEG-SEM, field-emission gun

703   scanning electron microscopy; SAXS, small angle x-ray

704   scattering; L, nanoparticles length; W, nanoparticles width; T,

705   nanoparticles thickness.

706

707   REFERENCES

708   1.   Dorozhkin, S. V. Nanosized and nanocrystalline calcium
709   orthophosphates. *Acta Biomater.* **2010**, *6*, 715-734.
710   2.   Al-Kattan, A.; Girod-Fullana, S.; Charvillat, C.; Ternet-
711   Fontebasso, H.; Dufour, P.; Dexpert-Ghys, J.; Santran, V.;
712   Bordre, J.; Pipy, B.; Bernad, J.; Drouet, C. Biomimetic
713   nanocrystalline apatites: Emerging perspectives in cancer
714   diagnosis and treatment. *Int. J. Pharm.* **2012**, *423*, 26-36.
715   3.   Epple, M.; Ganesan, K.; Heumann, R.; Klesing, J.; Kovtun, A.;
716   Neumann, S.; Sokolova, V. Application of calcium phosphate
717   nanoparticles in biomedicine. *J. Mater. Chem.* **2010**, *20*, 18-
718   23.
719   4.   Ali, I. New generation adsorbents for water treatment. *Chem.*
720   *Rev.* **2012**, *112*, 5073-5091.
721   5.   Kottegoda, N.; Munaweera, I.; Madusanka, N.; Karunaratne, V.
722   A green slow-release fertilizer composition based on urea-
723   modified hydroxyapatite nanoparticles encapsulated wood.
724   *Curr. Sci.* **2011**, 73-78.
725   6.   Mori, K.; Yamaguchi, K.; Hara, T.; Mizugaki, T.; Ebitani, K.;
726   Kaneda, K. Controlled synthesis of hydroxyapatite-supported
727   palladium complexes as highly efficient heterogeneous
728   catalysts. *J. Am. Chem. Soc.* **2002**, *124*, 11572-11573.
729   7.   Ferraz, M.; Monteiro, F.; Manuel, C. Hydroxyapatite
730   nanoparticles: a review of preparation methodologies. *J.*
731   *Appl. Biomater. Biomech.* **2004**, *2*, 74-80.
732   8.   Lin, K.; Wu, C.; Chang, J. Advances in synthesis of calcium
733   phosphate crystals with controlled size and shape. *Acta*
734   *Biomater.* **2014**, *10*, 4071-4102.
735   9.   Sadat-Shojai, M.; Khorasani, M.-T.; Dinpanah-Khoshdargi, E.;
736   Jamshidi, A. Synthesis methods for nanosized hydroxyapatite
737   with diverse structures. *Acta Biomater.* **2013**, *9*, 7591-7621.
738   10.   Newcomb, C. J.; Bitton, R.; Velichko, Y. S.; Snead, M. L.;
739   Stupp, S. I. The role of nanoscale architecture in
740   supramolecular templating of biomimetic hydroxyapatite
741   mineralization. *Small* **2012**, *8*, 2195-2202.

742   11.   Wang, A.; Yin, H.; Liu, D.; Wu, H.; Ren, M.; Jiang, T.; Cheng,
743   X.; Xu, Y. Size-controlled synthesis of hydroxyapatite
744   nanorods in the presence of organic modifiers. *Mater. Lett.*
745   **2007**, *61*, 2084-2088.
746   12.   Neira, I. S.; Kolen'ko, Y. V.; Lebedev, O. I.; Van Tendeloo,
747   G.; Gupta, H. S.; Guitián, F.; Yoshimura, M. An effective
748   morphology control of hydroxyapatite crystals via
749   hydrothermal synthesis. *Cryst. Growth Des.* **2008**, *9*, 466-474.
750   13.   Hu, Y.-Y.; Rawal, A.; Schmidt-Rohr, K. Strongly bound citrate
751   stabilizes the apatite nanocrystals in bone. *Proc. Natl.*
752   *Acad. Sci. U. S. A.* **2010**.
753   14.   Zipkin, I.; Gold, R. The citrate content of teeth. *Proc. Soc.*
754   *Exp. Biol. Med.* **1963**, *113*, 580-584.
755   15.   Delgado-López, J. M.; Frison, R.; Cervellino, A.;
756   Gómez-Morales, J.; Guagliardi, A.; Masciocchi, N. Crystal
757   Size, Morphology, and Growth Mechanism in Bio-Inspired Apatite
758   Nanocrystals. *Adv. Funct. Mater.* **2014**, *24*, 1090-1099.
759   16.   Delgado-López, J. M.; Iafisco, M.; Rodríguez, I.; Tampieri,
760   A.; Prat, M.; Gómez-Morales, J. Crystallization of
761   bioinspired citrate-functionalized nanoapatite with tailored
762   carbonate content. *Acta Biomater.* **2012**, *8*, 3491-3499.
763   17.   Sakhno, Y.; Ivanchenko, P.; Iafisco, M.; Tampieri, A.;
764   Martra, G. A step toward control of the surface structure of
765   biomimetic hydroxyapatite nanoparticles: effect of
766   carboxylates on the {010} P-rich/Ca-rich facets ratio. *J.*
767   *Phys. Chem. C* **2015**, *119*, 5928-5937.
768   18.   Chatzipanagis, K.; Iafisco, M.; Roncal-Herrero, T.; Bilton,
769   M.; Tampieri, A.; Kroger, R.; Delgado-Lopez, J. M.
770   Crystallization of citrate-stabilized amorphous calcium
771   phosphate to nanocrystalline apatite: a surface-mediated
772   transformation. *CrystEngComm* **2016**, *18*, 3170-3173.
773   19.   Iafisco, M.; Ramirez-Rodriguez, G. B.; Sakhno, Y.; Tampieri,
774   A.; Martra, G.; Gomez-Morales, J.; Delgado-Lopez, J. M. The
775   growth mechanism of apatite nanocrystals assisted by citrate:
776   relevance to bone biomineralization. *CrystEngComm* **2015**, *17*,
777   507-511.
778   20.   Martínez-Casado, F. J.; Iafisco, M.; Delgado-López, J. M.;
779   Martínez-Benito, C.; Ruiz-Pérez, C.; Colangelo, D.; Oltolina,
780   F.; Prat, M.; Gómez-Morales, J. Bioinspired Citrate–Apatite
781   Nanocrystals Doped with Divalent Transition Metal Ions.
782   *Cryst. Growth Des.* **2015**, *16*, 145-153.
783   21.   Delgado-López, J. M.; Iafisco, M.; Rodríguez-Ruiz, I.; Gómez-
784   Morales, J. Bio-inspired citrate-functionalized apatite thin
785   films crystallized on Ti–6Al–4V implants pre-coated with
786   corrosion resistant layers. *J. Inorg. Biochem.* **2013**, *127*,
787   261-268.

788 22. Šupová, M. Substituted hydroxyapatites for biomedical
789   applications: a review. *Ceram. Int.* **2015**, *41*, 9203-9231.
790 23. Iannotti, V.; Adamiano, A.; Ausanio, G.; Lanotte, L.;
791   Aquilanti, G.; Coey, J. M. D.; Lantieri, M.; Spina, G.;
792   Fittipaldi, M.; Margaris, G.; Trohidou, K.; Sprio, S.;
793   Montesi, M.; Panseri, S.; Sandri, M.; Iafisco, M.; Tampieri,
794   A. Fe-Doping-Induced Magnetism in Nano-Hydroxyapatites.
795   *Inorg. Chem.* **2017**, *56*, 4446-4458.
796 24. Ten Cate, J. M. Contemporary perspective on the use of
797   fluoride products in caries prevention. *Br. Dent. J.* **2013**,
798   *214*, 161-167.
799 25. Qu, H.; Wei, M. The effect of fluoride contents in fluoridated
800   hydroxyapatite on osteoblast behavior. *Acta Biomater.* **2006**,
801   *2*, 113-119.
802 26. Wiegand, A.; Buchalla, W.; Attin, T. Review on fluoride-
803   releasing restorative materials—fluoride release and uptake
804   characteristics, antibacterial activity and influence on
805   caries formation. *Dent. Mater.* **2007**, *23*, 343-362.
806 27. Ten Cate, J.; Featherstone, J. Mechanistic aspects of the
807   interactions between fluoride and dental enamel. *Crit. Rev.
808   Oral Biol. Med.* **1991**, *2*, 283-296.
809 28. Sun, R.; Chen, K.; Wu, X.; Zhao, D.; Sun, Z. Controlled
810   synthesis and enhanced luminescence of europium-doped
811   fluorine-substituted hydroxyapatite nanoparticles.
812   *CrystEngComm* **2013**, *15*, 3442-3447.
813 29. Wang, L.; Wang, M.; Li, M.; Shen, Z.; Wang, Y.; Shao, Y.;
814   Zhu, Y. Trace fluorine substituted calcium deficient
815   hydroxyapatite with excellent osteoblastic activity and
816   antibacterial ability. *CrystEngComm* **2018**, *20*, 5744-5753.
817 30. Chen, H.; Sun, K.; Tang, Z.; Law, R. V.; Mansfield, J. F.;
818   Czajka-Jakubowska, A.; Clarkson, B. H. Synthesis of
819   fluorapatite nanorods and nanowires by direct precipitation
820   from solution. *Cryst. Growth Des.* **2006**, *6*, 1504-1508.
821 31. Nathanael, A. J.; Mangalaraj, D.; Hong, S.; Masuda, Y.; Rhee,
822   Y.; Kim, H. Influence of fluorine substitution on the
823   morphology and structure of hydroxyapatite nanocrystals
824   prepared by hydrothermal method. *Mater. Chem. Phys.* **2013**,
825   *137*, 967-976.
826 32. Jha, L.; Best, S.; Knowles, J.; Rehman, I.; Santos, J. D.;
827   Bonfield, W. Preparation and characterization of fluoride-
828   substituted apatites. *J. Mater. Sci.: Mater. Med.* **1997**, *8*,
829   185-191.
830 33. Roche, K. J.; Stanton, K. T. Measurement of fluoride
831   substitution in precipitated fluorhydroxyapatite
832   nanoparticles. *J. Fluorine Chem.* **2014**, *161*, 102-109.

833   34.   Rodríguez-Lorenzo, L. M.; Hart, J. N.; Gross, K. A. Structural
834   and   chemical   analysis   of   well-crystallized
835   hydroxyfluorapatites. *J. Phys. Chem. B* **2003**, *107*, 8316-8320.
836   35.   Gómez Morales, J.; Fernández Penas, R.; Verdugo-Escamilla,
837   C.; Degli Esposti, L.; Oltolina, F.; Prat, M.; Iafisco, M.;
838   Fernández Sánchez, J. Bioinspired Mineralization of Type I
839   Collagen Fibrils with Apatite in Presence of Citrate and
840   Europium Ions. *Crystals* **2019**, *9*, 13.
841   36.   Gómez-Morales, J.; Verdugo-Escamilla, C.; Fernández-Penas,
842   R.; Parra-Milla, C. M.; Drouet, C.; Maube-Bosc, F.; Oltolina,
843   F.; Prat, M.; Fernández-Sánchez, J. F. Luminescent biomimetic
844   citrate-coated   europium-doped   carbonated   apatite
845   nanoparticles for use in bioimaging: physico-chemistry and
846   cytocompatibility. *RSC Adv.* **2018**, *8*, 2385-2397.
847   37.   Dorozhkin, S. V. Calcium orthophosphates (CaPO4): occurrence
848   and properties. *Prog. Biomater.* **2016**, *5*, 9-70.
849   38.   Free, A. H. The citrate content of whole teeth, dentin and
850   enamel. *J. Dent. Res.* **1943**, *22*, 477-478.
851   39.   Coelho, A. Topas Academic V5. *Coelho Software* **2012**.
852   40.   Hughes, J. M.; Cameron, M.; Crowley, K. D. Structural
853   variations in natural F, OH, and Cl apatites. *Am. Mineral.*
854   **1989**, *74*, 870-876.
855   41.   Abràmoff, M. D.; Magalhães, P. J.; Ram, S. J. Image processing
856   with ImageJ. *Biophotonics Intern.* **2004**, *11*, 36-42.
857   42.   Brunauer, S.; Emmett, P. H.; Teller, E. Adsorption of gases
858   in multimolecular layers. *J. Am. Chem. Soc.* **1938**, *60*, 309-
859   319.
860   43.   Hammersley, A. FIT2D: an introduction and overview. *ESFR
861   Internal Report ESRF97HA02T* **1997**, *68*, 58.
862   44.   Kotlarchyk, M.; Chen, S. H. Analysis of small angle neutron
863   scattering spectra from polydisperse interacting colloids. *J.
864   Chem. Phys.* **1983**, *79*, 2461-2469.
865   45.   Kotlarchyk, M.; Stephens, R. B.; Huang, J. S. Study of Schultz
866   distribution   to   model   polydispersity   of   microemulsion
867   droplets. *J. Phys. Chem.* **1988**, *92*, 1533-1538.
868   46.   Nallet, F.; Laversanne, R.; Roux, D. Modelling X-ray or
869   neutron scattering spectra of lyotropic lamellar phases:
870   interplay between form and structure factors. *J. Phys. II*
871   **1993**, *3*, 487-502.
872   47.   Rameshbabu, N.; Kumar, T. S.; Rao, K. P. Synthesis of
873   nanocrystalline   fluorinated   hydroxyapatite   by   microwave
874   processing and its in vitro dissolution study. *Bull. Mater.
875   Sci.* **2006**, *29*, 611-615.
876   48.   Venkateswarlu, K.; Sreekanth, D.; Sandhyarani, M.;
877   Muthupandi, V.; Bose, A.; Rameshbabu, N. X-ray peak profile
878   analysis of nanostructured hydroxyapatite and fluorapatite.
879   *Int. J. Biosci., Biochem. Bioinf.* **2012**, *2*, 389-393.

880   49.   Rodrıguez-Lorenzo, L.; Hart, J.; Gross, K. Influence of
881   fluorine in the synthesis of apatites. Synthesis of solid
882   solutions of hydroxy-fluorapatite. *Biomaterials* **2003**, *24*,
883   3777-3785.
884   50.   Tonsuaadu, K.; Gross, K. A.; Plūduma, L.; Veiderma, M. A
885   review on the thermal stability of calcium apatites. *J. Therm.*
886   *Anal. Calorim.* **2011**, *110*, 647-659.
887   51.   Rey, C.; Combes, C.; Drouet, C.; Sfihi, H.; Barroug, A.
888   Physico-chemical properties of nanocrystalline apatites:
889   implications for biominerals and biomaterials. *Mater. Sci.*
890   *Eng. C* **2007**, *27*, 198-205.
891   52.   Di Mauro, V.; Iafisco, M.; Salvarani, N.; Vacchiano, M.;
892   Carullo, P.; Ramírez-Rodríguez, G. B.; Patrício, T.;
893   Tampieri, A.; Miragoli, M.; Catalucci, D. Bioinspired
894   negatively charged calcium phosphate nanocarriers for cardiac
895   delivery of MicroRNAs. *Nanomedicine* **2016**, *11*, 891-906.
896   53.   Koutsopoulos, S. Synthesis and characterization of
897   hydroxyapatite crystals: a review study on the analytical
898   methods. *J. Biomed. Mater. Res.* **2002**, *62*, 600-612.
899   54.   Antonakos, A.; Liarokapis, E.; Leventouri, T. Micro-Raman and
900   FTIR studies of synthetic and natural apatites. *Biomaterials*
901   **2007**, *28*, 3043-3054.
902   55.   Ivanchenko, P.; Delgado-López, J. M.; Iafisco, M.; Gómez-
903   Morales, J.; Tampieri, A.; Martra, G.; Sakhno, Y. On the
904   surface effects of citrates on nano-apatites: evidence of a
905   decreased hydrophilicity. *Sci. Rep.* **2017**, 7, 8901.
906   56.   Wu, Y.-J.; Tseng, Y.-H.; Chan, J. C. Morphology control of
907   fluorapatite crystallites by citrate ions. *Cryst. Growth Des.*
908   **2010**, *10*, 4240-4242.
909   57.   Zhang, H. G.; Zhu, Q. Surfactant-assisted preparation of
910   fluoride-substituted hydroxyapatite nanorods. *Mater. Lett.*
911   **2005**, *59*, 3054-3058.
912   58.   Selvig, K. A. Periodic lattice images of hydroxyapatite
913   crystals in human bone and dental hard tissues. *Calcif. Tissue*
914   *Res.* **1970**, *6*, 227-238.
915   59.   Miake, Y.; Aoba, T.; Moreno, E.; Shimoda, S.; Prostak, K.;
916   Suga, S. Ultrastructural studies on crystal growth of
917   enameloid minerals in elasmobranch and teleost fish. *Calcif.*
918   *Tissue Int.* **1991**, *48*, 204-217.

919

920

921

922

923

924

925

926

927

928

929

930

931   **For Table of Contents Only**

932   **Manuscript Title:** "Combined effect of citrate and fluoride ions on

933   hydroxyapatite nanoparticles"

934   **Authors:** Lorenzo Degli Esposti, Alessio Adamiano, Anna Tampieri,

935   Gloria Belen Ramirez-Rodriguez, Dritan Siliqi, Cinzia Giannini,

936   Pavlo Ivanchenko, Gianmario Martra, Feng-Huei Lin, José Manuel

937   Delgado-López, Michele Iafisco

938   **Table of Contents Graphic:**

Bio-inspired crystallization

Citrate

Fluorine

F⁻

50 nm

Citrate-fluorhydroxyapatite
Flattened rods

939

940

Synopsis: Citrate-fluoride-hydroxyapatite (citrate-FHA) nanoparticles were prepared in order to assess the combined effect of citrate and fluoride ions on HA. Citrate-FHA exhibits a flattened hexagonal rod-like morphology in contrast to the needle-like platelet morphology of citrate-HA. The density of surface citrates and the relative amount of unidentate citrate–Ca^{2+} adducts *vs* the ionic-like ones is higher for citrate-FHA than for citrate-HA.
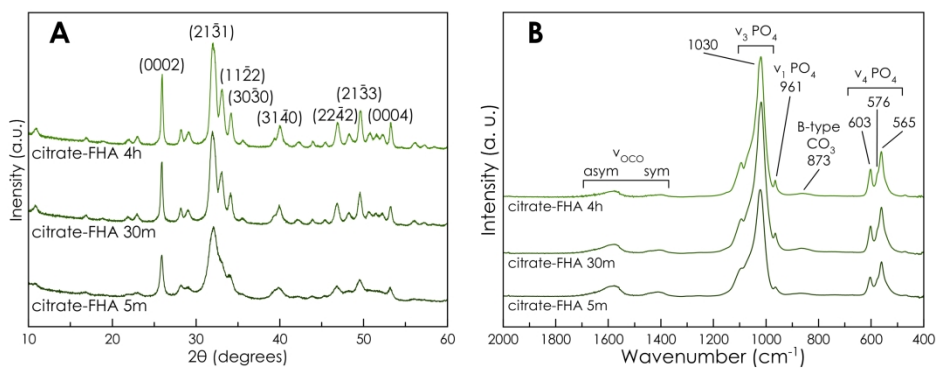
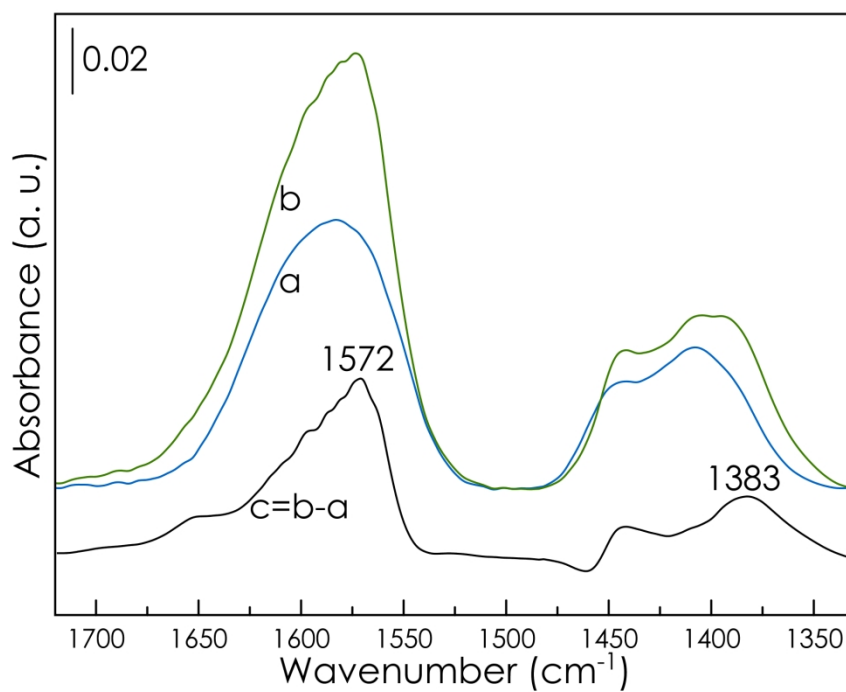Figure 1. (A) PXRD patterns and (B) IR-ATR of citrate-FHA 5m, citrate-FHA 30m, and citrate-FHA 4h.

Figure 2. FT-IR spectra of citrate-HA 4h (a) and citrate-FHA 4h (b) after exchange with D2O and subsequent 60 min outgassing at b.t., the spectra are normalized by mass of sample and SSA of the material; curve (c) resulting from the difference (b)-(a).
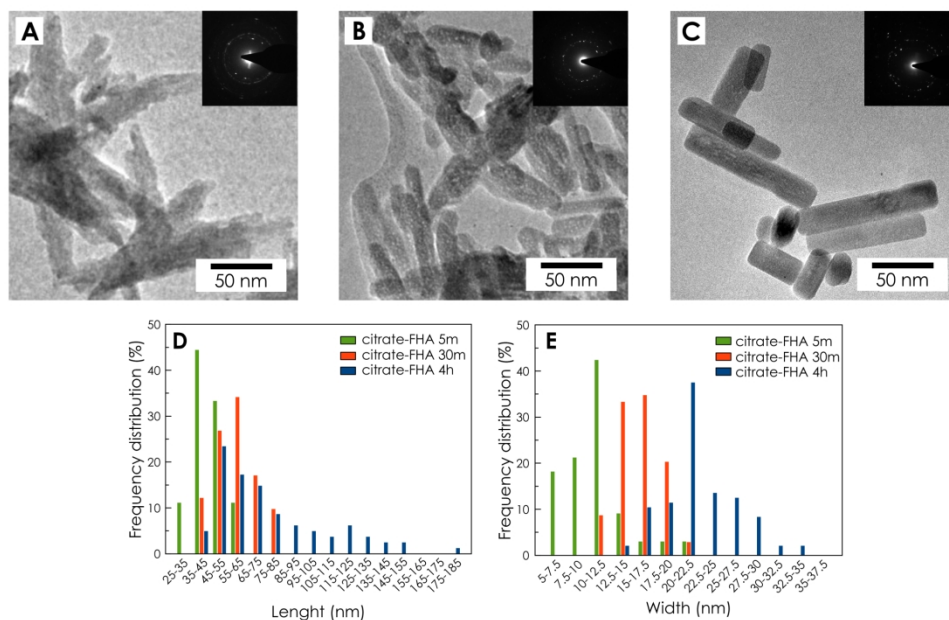
186x139mm (300 x 300 DPI)

Figure 3. (A-C) TEM micrographs of (A) citrate-FHA 5m, (B) citrate-FHA 30m and (C) citrate-FHA 4h. Insets show the relative SAED pattern. (D-E) Histograms of the distributions of (D) width and (E) length of citrate-FHA 5m, citrate-FHA 30m, and citrate-FHA 4h (blue bars).
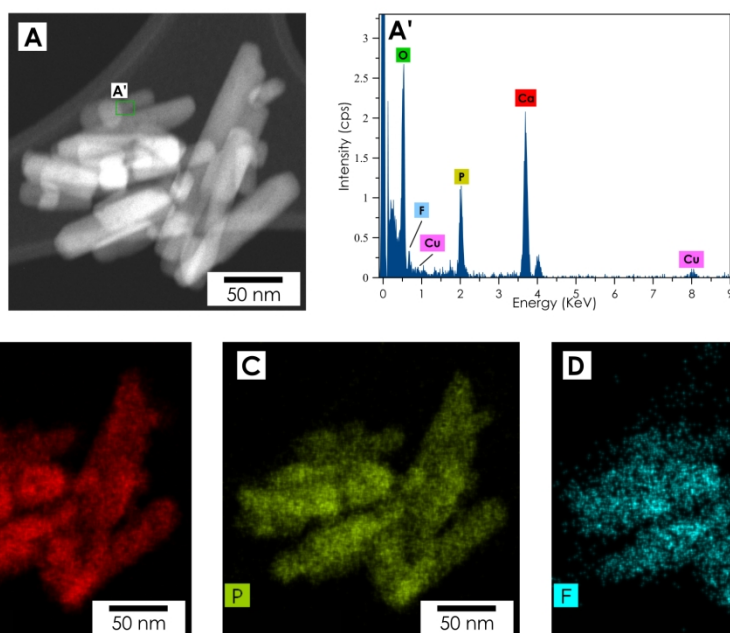
Figure 4. (A) STEM-HAADF micrograph of citrate-FHA 4h, (A') EDS spectrum from area marked in (A), and chemical maps of Ca (B), P (C), and F (D) from the same micrograph reported in (A). In (A'), the Cu peaks are due to the sample holder.
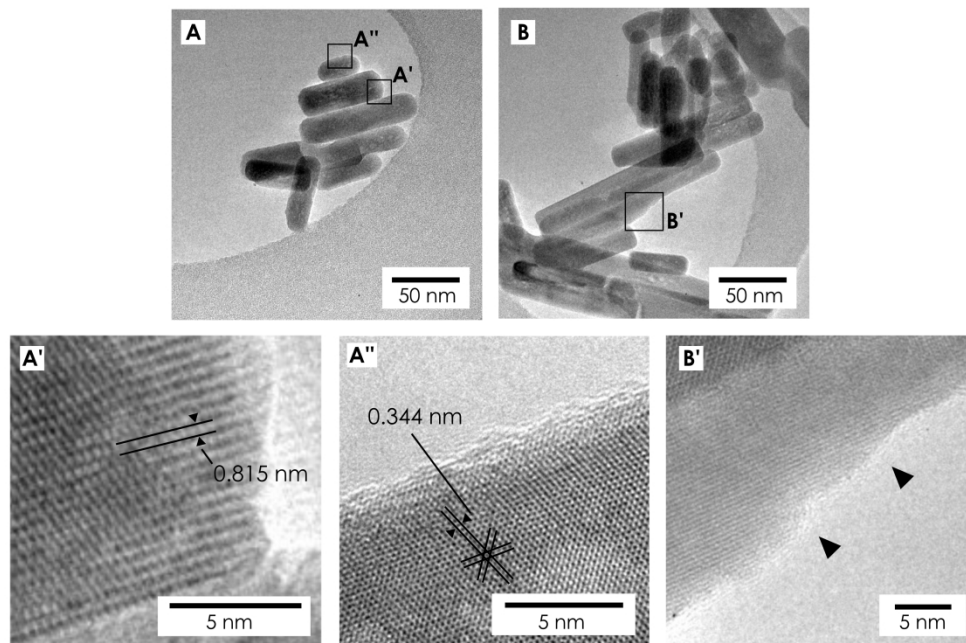
Figure 5. HR-TEM micrographs of citrate-FHA 4h. A', A'', and B' correspond to the high magnification of the portions enframed within the black squares in micrographs A and B, respectively. (A') 0.815 nm fringes that run along citrate-FHA 4h nanocrystal length, (A'') hexagonal fringe pattern with 0.344 spacing, and (B') stepped surfaces (marked by arrows) along a-b planes.
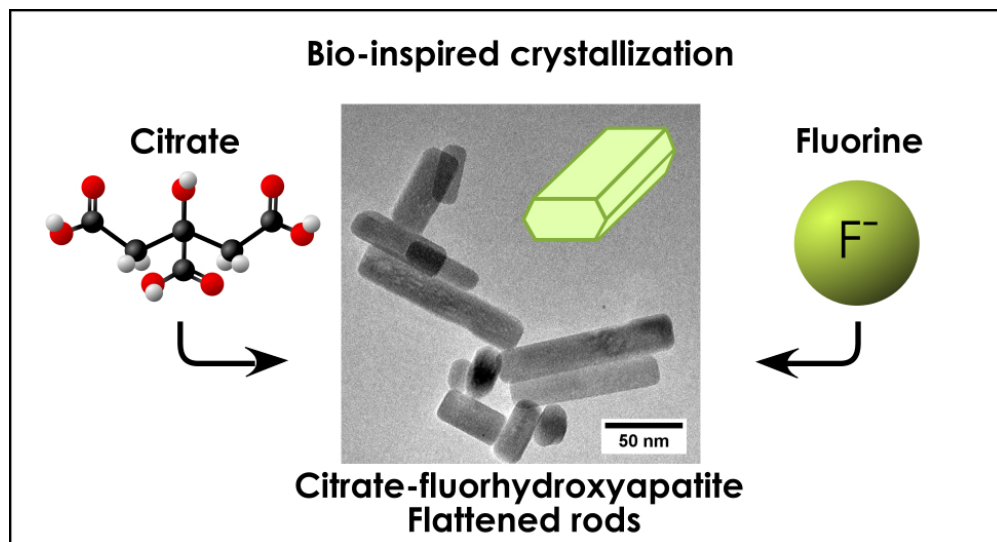
Bio-inspired crystallization

Citrate

Fluorine

F^-

Citrate-fluorhydroxyapatite
Flattened rods

Table of contents